

<https://doi.org/10.1038/s41612-024-00627-z>

Future changes in the wintertime ENSO-NAO teleconnection under greenhouse warming

Xin Geng¹, Jong-Seong Kug²✉ & Yu Kosaka³

El Niño–Southern Oscillation (ENSO) teleconnection to the Euro–Atlantic exhibits strong subseasonal variations, as the North Atlantic Oscillation (NAO) response systematically reverses its phase from early to late winter. Based on two sets of atmospheric model simulations in CMIP6 forced by historical and projected SST, we report a future disappearance of this teleconnection reversal, with the positive early winter ENSO–NAO correlation turning negative and the negative late winter correlation becoming stronger. We suggest that this negative NAO tendency is associated with the strengthening and eastward shift of the ENSO atmospheric teleconnection towards the Euro–Atlantic due to parallel changes in the ENSO tropical convection. While the early winter NAO phase transition is further facilitated by the mean state change in the North Atlantic jet meridional shear, which shifts the ENSO-driven Rossby wave-propagating direction, an intensified stratospheric pathway is demonstrated to play an additional role in strengthening the late winter NAO response.

As one of the most prominent components of the climate system, the El Niño–Southern Oscillation (ENSO) excites various teleconnections that affect the seasonal-to-interannual climate variabilities around the globe^{1,2}. In contrast to regions such as the North Pacific and North America, ENSO effects over the remote Euro–Atlantic sector are relatively fragile and controversial³. Although an out-of-phase North Atlantic Oscillation (NAO) anomaly is detected during ENSO late winter (January–March, JFM), which makes ENSO an important source of seasonal predictability in the Euro–Atlantic region⁴, the connection is relatively weak and characterized by a high degree of uncertainty^{5–7} due to large local internal atmospheric variabilities⁸. It has been found that the ENSO–NAO relationship changes nonlinearly with ENSO strength^{9–11}, is sensitive to ENSO flavors^{12,13}, and shows significant subseasonal variations from November to March^{14–16}. In early winter (November–December), a positive NAO pattern can be observed during a warm ENSO event^{16,17}. After early January, however, the response abruptly reverses its sign¹⁸, and a negative NAO pattern is generated thereafter^{19,20}.

To understand the aforementioned ENSO–NAO linkage, many mechanisms have been proposed. The physical processes involved in the early winter ENSO–NAO teleconnection are generally different from those in the late winter. During El Niño/La Niña early winter, the influence is mostly contributed by the strong convection anomalies in the tropical

Indian–Pacific Ocean^{16–18,21} and/or the Gulf of Mexico–Caribbean Sea^{15,22}, which could excite Rossby wave trains that reach the North Atlantic and then lead to a positive/negative NAO anomaly. However, due to the climatological weakening of the North Atlantic jet meridional shear in early January, the horizontal structure (i.e., tilt direction) of the ENSO-related Rossby waves over northeastern North America changes, thus shifting the propagation direction from northeast to southeast¹⁸. An abrupt NAO phase reversal then occurs¹⁸ with the amplification effect of the North Atlantic eddy–low frequency feedback^{23,24}.

The negative/positive NAO response is then maintained during El Niño/La Niña late winter by several mechanisms. First, the ENSO-related delayed tropical North Atlantic (TNA) sea surface temperature (SST) or precipitation anomalies may exert a modulating effect on the NAO atmospheric circulation^{9,10,25–27}. Also, the ENSO-induced tropical central-eastern Pacific convection anomalies strengthen during this period and start playing an overwhelming role in generating low-frequency Rossby waves or transient eddies propagating downstream from the North Pacific to the North Atlantic, which in turn gives rise to a negative/positive NAO pattern^{20,28}. In addition, a chain of stratospheric processes emerges as another key mechanism that works together with the aforementioned tropospheric pathways^{15,20}. Under El Niño conditions, the deepened Aleutian low that is associated with the amplification of wavenumber-1 and enhanced wave

¹CIC-FEMD/ILCEC, Key Laboratory of Meteorological Disaster of Ministry of Education (KLME), Nanjing University of Information Science and Technology, Nanjing, China. ²School of Earth and Environmental Sciences, Seoul National University, Seoul, South Korea. ³Research Center for Advanced Science and Technology, The University of Tokyo, Tokyo, Japan. ✉e-mail: jkskug1@gmail.com

activity upward propagation into the lower stratosphere leads to deceleration of the stratospheric polar vortex²⁹. These stratospheric circulation anomalies then propagate downward and result in a subsequent late winter-negative NAO anomaly^{19,30,31}. The opposite generally happens during La Niña conditions, particularly for strong events^{29,32}.

Although the historical ENSO teleconnection to the NAO has been extensively studied, there still exists a lack of understanding as to whether or not the present-day (PD) teleconnection evolutionary features will persist under future greenhouse warming. While the future change in ENSO SST characteristics remains a matter of debate, the tropical precipitation responses to ENSO are projected to be more robust and eastward shifting^{33–37}, with more extreme ENSO rainfall variability^{38,39}. Given this, one might expect a future change in the ENSO-NAO teleconnection. During the late winter, this connection is indeed shown to be strengthened by the analyses of the multiple historical and RCP8.5 scenario CMIP5 simulations⁴⁰ and also several single coupled model projections^{41–44}. However, ENSO SST and precipitation patterns in coupled models suffer from some common biases such as the excessive westward extension of ENSO SST variability into the western Pacific compared to observation^{45–47}. This spatial systematic error largely limits the realistic representation and future projection of the ENSO extratropical teleconnections^{48,49}. In addition, unlike the late winter ENSO-NAO teleconnection, future changes in the early winter ENSO influence on the NAO and the subseasonal teleconnection reversal that occurs in early January have not been investigated. Thus this paper focuses on these scientific issues based on two sets of atmospheric model experiments in CMIP6. Namely, “AMIP”, forced by observed PD SST (also denoted as ‘AMIP-PD’ in this study), and “AMIP-future4K”, forced by observed SST plus spatially patterned future SST warming. On the one hand, this guarantees a relatively realistic SST pattern that can effectively exclude the possible interference caused by the SST modeling bias. On the other hand, our previous study has already suggested that the multi-model ensemble mean of the AMIP-PD simulations can well reproduce the observed wintertime ENSO-NAO relationship, including the subseasonal transition that occurs in early January¹⁸. Therefore, it is reasonable to examine the future changes of the teleconnection by analyzing the difference between the AMIP-future4K and AMIP-PD simulations. The possible mechanisms responsible for the changes in the teleconnection are also discussed. In the remainder of the article, Section 2 presents results and possible mechanisms, Section 3 provides conclusions and discussions, and Section 4 describes data and method.

Results

Future changes in the wintertime ENSO-NAO teleconnection

In Fig. 1a, we first display the regressed wintertime Euro-Atlantic zonal mean (80°W–30°E) daily sea level pressure (SLP) anomalies with respect to the DJF Niño-3.4 index in observations. It shows that, during an El Niño winter, there appears a prominent NAO phase reversal from positive to negative in early January. While a significant positive NAO pattern is detected in the early winter (November 1 to January 7, also denoted as P1) (Fig. 1e), the late winter features an evident negative NAO pattern (after January 9, also denoted as P2) (Fig. 1f). This observed subseasonal phase reversal of the ENSO-NAO relationship can be realistically reproduced by the multi-model ensemble mean (MME) of the AMIP-PD simulations (Fig. 1b), in agreement with our previous study¹⁸, although the amplitude seems to be weaker⁵⁰. It is thus reasonable to use the AMIP-PD simulations as a reference to investigate the future change in this teleconnection. When the future projected SST warming pattern is added to the boundary forcing in the AMIP-future4K experiments, remarkable changes are detected in the North Atlantic atmospheric responses to ENSO (Fig. 1c, d). In P2, the negative NAO response to ENSO is evidently strengthened in the future (Fig. 1i), which is consistent with previous results based on the CMIP5 RCP8.5 simulations⁴⁰. However, in P1, the PD positive NAO response switches to negative in the AMIP-future4K simulations (Fig. 1h). In other words, the greenhouse warming-induced SST warming pattern favors the establishment of the negative NAO response in both ENSO early and late

winter (Fig. 1d, k and l), which corresponds to the phase reversal of the early winter NAO response and the strengthening of the late winter NAO anomaly. And the PD subseasonal reversal of the ENSO-NAO phase relationship naturally disappears under the future greenhouse warming.

Some studies argue that the Euro-Atlantic early winter response to ENSO is also similar to the East Atlantic pattern^{51,52}, which is often interpreted as a southward-shifted NAO. Although the ENSO-regressed spatial distribution (Fig. 1e) projects both the NAO and the East Atlantic pattern, these two modes are orthogonal, and the character of the NAO evolution and its future change in response to ENSO remains basically unchanged even when the East Atlantic pattern is considered.

Consistent with the NAO, the ENSO-related surface climate anomalies in the Euro-Atlantic region also show corresponding future changes (Fig. 2). Compared to the PD, El Niño events under future greenhouse warming, both during P1 and P2, are accompanied by colder SAT in northwestern Europe due to the changes in more northerly winds, and warmer SAT in northeastern North America and North Africa as a result of the southerly wind tendency. Meanwhile, precipitation is reduced in the subpolar North Atlantic and increased in the subtropics. These distributions are in good agreement with the climate traces of the winter anomalous negative NAO pattern^{53,54}, further confirming that the future change in the ENSO-NAO teleconnection is robust.

Possible mechanisms for future teleconnection changes

We now turn to explore the possible mechanisms responsible for these aforementioned future changes. Since the PD NAO responses to ENSO in P1 are opposite to those in P2, the mechanisms are investigated separately. The ENSO-regressed tropical precipitation during P1 and P2 for the two experiments (Fig. 3a–d) are examined first because ENSO teleconnections to the extratropical region are generally bridged by the ENSO-induced tropical convection anomalies^{55,56}. In PD, El Niño P1 is accompanied by reduced precipitation in the western Pacific and enhanced precipitation in the central-eastern Pacific and western Indian Ocean. The response in P2 is similar to that in P1 but with a slightly strengthened magnitude. However, when comparing the responses between the two simulations, we find that, in both P1 and P2, the ENSO-induced tropical precipitation anomaly is significantly strengthened and extends more eastward in the future simulations, especially in the Pacific sector. To further show this, we examine the intensity and zonal location of the ENSO-regressed tropical (5°S–5°N) central-eastern Pacific precipitation anomaly in the two experiments (Fig. 3e, f). The zonal location is defined as the longitude of the maximum regressed tropical (5°S–5°N) Pacific precipitation anomaly. Compared to that in the PD, the precipitation anomaly in the AMIP-future4K simulations is much stronger and shifted more eastward by about 20 degrees longitude. Similar change can also be detected in terms of the negative precipitation response in the western Pacific (Supplementary Fig. 1) and the positive precipitation response in the western Indian Ocean (Supplementary Fig. 2). These results are fundamentally consistent with previous studies, which suggest that although changes in ENSO SST properties are uncertain and appear to be highly model-dependent in future scenarios, an enhanced and eastward-shifted ENSO convection response in the tropics is relatively certain^{34–36}.

In response to the strengthened and eastward-shifted tropical convection anomalies, the future changes in the ENSO extratropical atmospheric teleconnections are expected to show similar features. To examine this, ENSO-regressed 250-hPa geopotential height anomalies for P1 and P2 based on the two simulations are displayed (Fig. 4). The associated WAF is also shown to illustrate the wave energy propagation. In the AMIP-PD simulations, the Rossby wave train propagates poleward and eastward from the tropical Indian Ocean and tropical central Pacific to the North Atlantic (Fig. 4a, b). Over northeastern North America, it propagates northeastward in early winter (Fig. 4a) but southeastward in late winter (Fig. 4b). This corresponds well to the NAO phase transition from positive in P1 to negative in P2, as suggested by our previous study¹⁸. In the AMIP-future4K simulations, the Rossby wave train associated with the ENSO-related

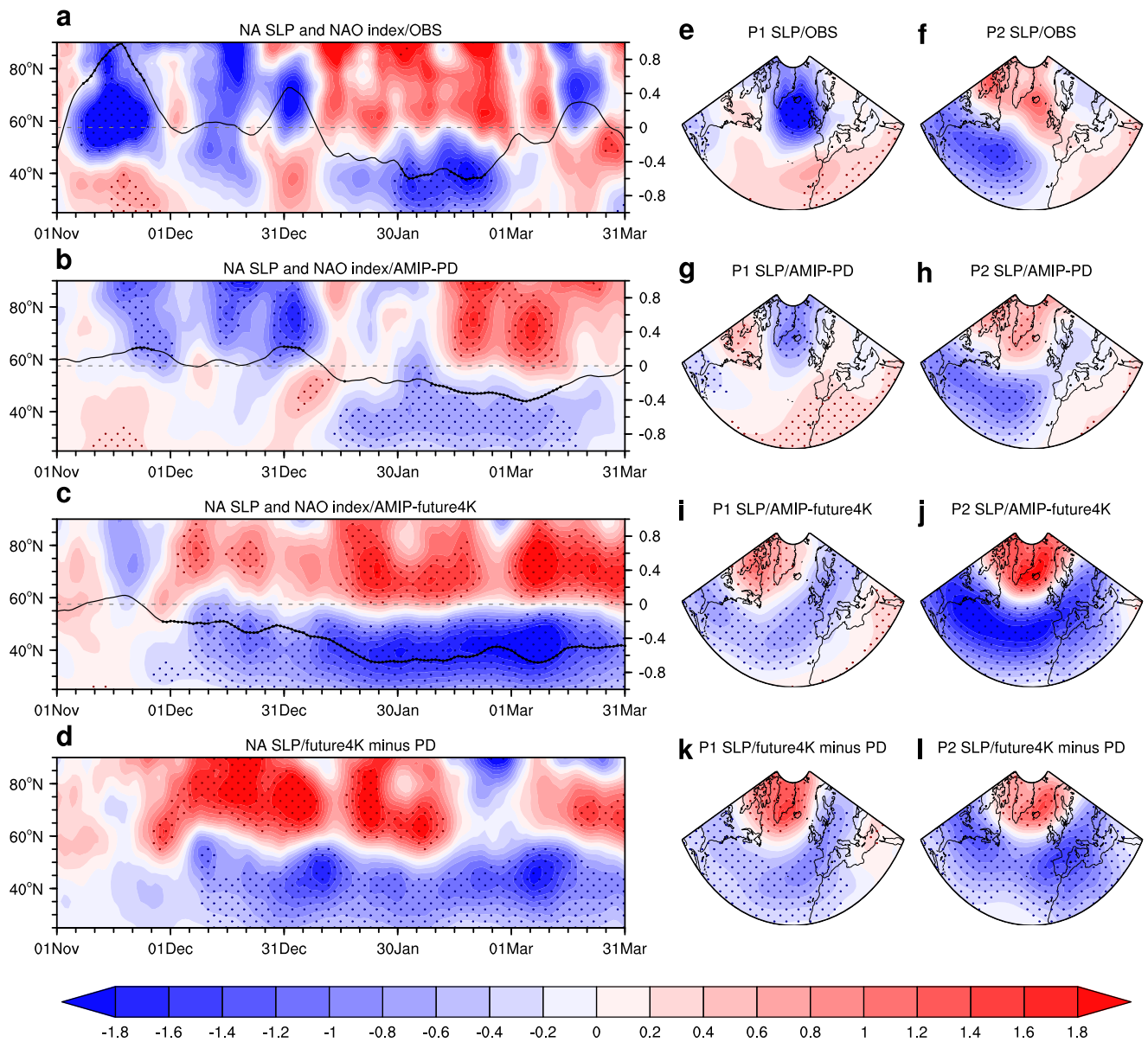


Fig. 1 | Future changes in the wintertime ENSO-NAO teleconnection. Regression coefficients of the wintertime North Atlantic zonal mean (80°W–30°E) daily SLP (shadings in hPa) and NAO index (black curve) with respect to the DJF Niño-3.4 index for (a) observations and the multi-model ensemble mean (MME) of the (b) AMIP-PD, (c) AMIP-future4K simulations and (d) the differences between the AMIP-future4K and AMIP-PD simulations. Regression coefficients of the (e) P1

(November 1 to January 7) and (f) P2 (January 9 to March 31) North Atlantic SLP anomalies with respect to the DJF Niño-3.4 index for observations. **g–l** are the same as (e, f) but for the MME of AMIP-PD simulations, AMIP-future4K simulations and the differences between the AMIP-future4K and AMIP-PD simulations, respectively. The dots denote the corresponding anomalies that are significant at the 90% confidence level.

tropical convection anomaly is also evident. Compared to those in the PD, the geopotential height anomalies embedded in the Rossby wave train in the future simulations intensify and move eastward during both P1 and P2, consistent with the changes in the tropical convection. In this case, the positive geopotential anomalies over the northeastern North America strengthen and extend eastward into the subpolar North Atlantic region, thus favoring the establishment of a negative NAO pattern. To further illustrate this argument, we examine the relationship between the intensity and zonal location of the tropical central-eastern Pacific convection anomaly during P1 and P2 of ENSO winters with the concurrent NAO response (Fig. 5). Regarding the influence of precipitation intensity, except for the positive correlation between the precipitation intensity and NAO in PD P1 (Fig. 5a), which reflects the coincident positive ENSO-NAO relationship, negative correlations are found for PD P2 and for both P1 and P2 in the AMIP-future4K simulations (Fig. 5a, b). There are also negative

correlations between the zonal location of the tropical central-eastern Pacific convection and the NAO response during ENSO winters in both experiments (Fig. 5c, d), although the correlation is insignificant. These results suggest that as the tropical Pacific convection becomes stronger and shifts eastward, more negative NAO response tends to be generated. As a consequence, this change makes it easier for the PD positive NAO response to weaken and even turn negative in early winter, but further strengthens the negative NAO response in late winter in the future.

However, the negative correlations between the ENSO-induced tropical convection intensity and zonal location with the NAO responses are not always significant (Fig. 5), indicating the potential influence of other mechanisms. In Fig. 4, in addition to the strengthening and eastward shift of the ENSO teleconnection, we observe another distinct feature between the two experiments in P1. Over northeastern North America, the Rossby wave propagates northeastward in the AMIP-PD simulations (Fig. 4a) but

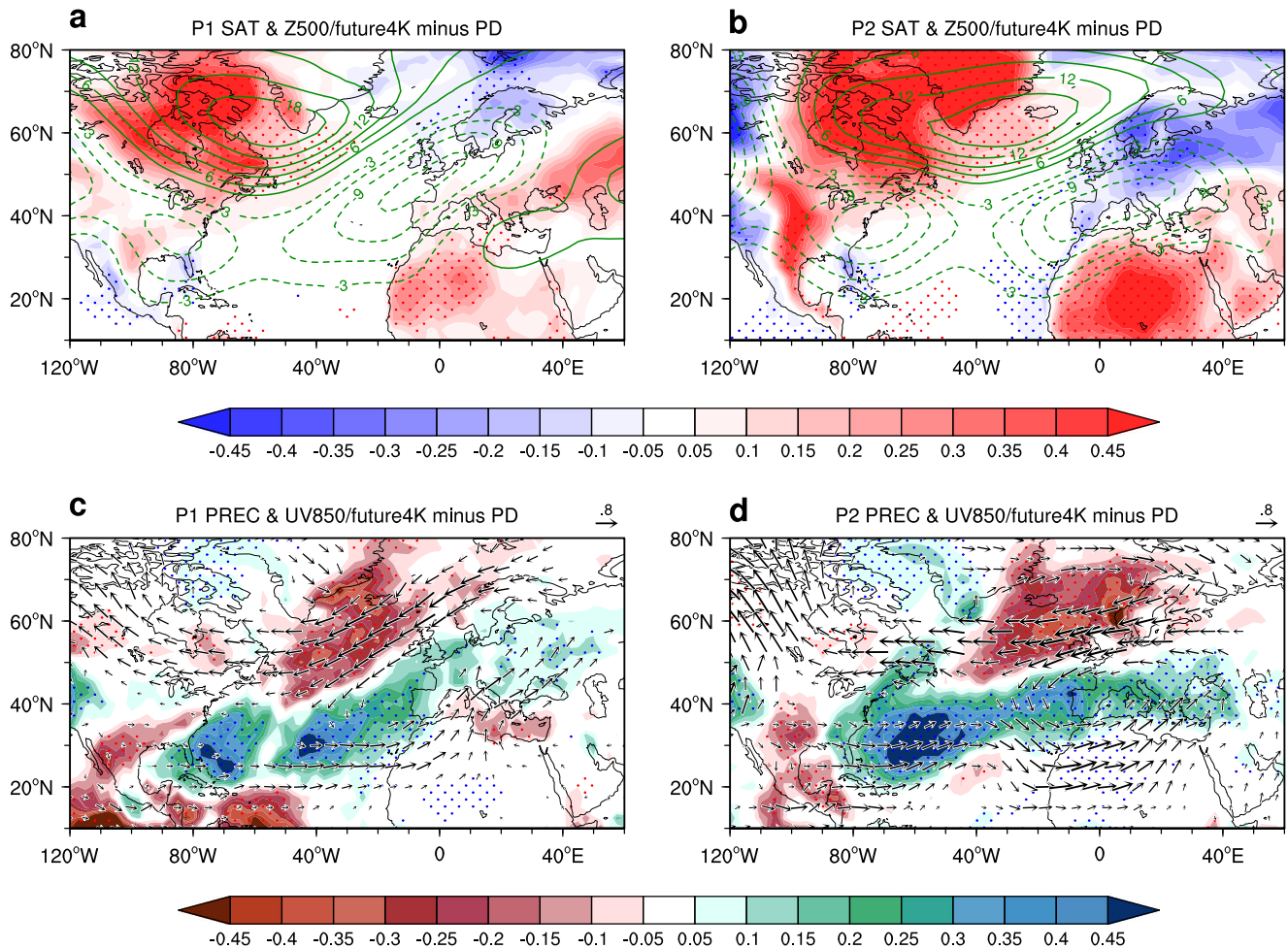


Fig. 2 | Future changes in the wintertime ENSO climate response in the Euro-Atlantic sector. Regression coefficients of the (a) P1 and (b) P2 North Atlantic SAT (shadings in K) and 500-hPa geopotential height (contours in m) anomalies with respect to the DJF Niño-3.4 index for the difference between the MME of the AMIP-future4K and AMIP-PD simulations. c, d are the same as a, b but for the precipitation

(shadings in mmday^{-1}) and 850-hPa horizontal wind (vectors in ms^{-1}) anomalies. The dots denote the surface climate anomalies that are significant at the 90% confidence level. Note the wind anomaly is shown only when its zonal or meridional component is significant at the 90% confidence level.

southeastward in the AMIP-future4K simulations (Fig. 4c). This leads to the downstream negative geopotential height anomaly shifting from the north to south, which effectively makes the PD early winter positive NAO response to weaken and even turn negative in the future.

Because the propagating direction shift is confined mostly to the meridional component of the WAF (i.e., F_y), we then decompose the P1 F_y over the target region into four terms for these two simulations. The latitudinal distributions of the F_y and its four constituents are displayed in Fig. 6a, b. As we can see, F_y over northeastern North America is positive in AMIP-PD simulations but negative in AMIP-future4K simulations, which corresponds well to the northward and southward WAF propagation in these two experiments. Whereas ‘term2’, ‘term 3’, and ‘term 4’ are small, ‘term 1’ shows larger amplitudes and is primarily responsible for the F_y anomalies. According to Eq. (2), the energy propagation associated with ‘term 1’ depends on $-u'v'$, which is further determined by the horizontal structure of the geopotential height anomaly. If the anomaly shows an isotropic structure (i.e., $-u'v' \approx 0$), the wave energy will hardly propagate meridionally. If the anomaly pattern is deformed to have a northwest-southeast tilt, this term will be positive (i.e., $-u'v' > 0$) and therefore will prompt the Rossby wave energy to head northward. On the contrary, it will propagate southward if the anomaly has a northeast-southwest tilt (i.e., $-u'v' < 0$). This is confirmed by the spatial patterns of the ENSO-related atmospheric anomalies over the northeastern North American region (Fig. 4a, c). We indeed observe that the positive

geopotential anomalies over the target region exhibit a northwest-southeast tilt in the AMIP-PD simulations but show a northeast-southwest tilt in the AMIP-future4K simulations (blue lines in Fig. 4a, c).

We further suggest that the change in the teleconnection horizontal structure is in turn associated with the atmospheric mean state alteration between the two experiments. In the PD, the upper troposphere exists an evident Atlantic jet over the western Atlantic region, with a central wind speed higher than 40 ms^{-1} . To the north of this Atlantic jet, the westerly wind speed decreases with latitude (Fig. 6c). Over northeastern North America, the westerly is therefore stronger in the south and relatively weaker in the north, which is conducive to forming atmospheric anomalies with a northwest-southeast tilt. From PD to the future, however, the westerly wind speed accelerates at about 55°N but decelerates at about 40°N as a result of the poleward shift of the North Atlantic jet due to the greenhouse warming⁵⁷⁻⁵⁹. This climatological change weakens the meridional shear of the Atlantic jet at its northern edge, which forces the atmospheric anomaly to tilt in a northeast-southwest direction (Fig. 4) and eventually leads to the phase reversal of the NAO response. An alternative explanation for this mean state modulation is that the future change in the zonal wind climatology over the northern edge of the North Atlantic jet (Fig. 6c) may reduce the turning latitude of the Rossby wave⁶⁰, causing the wave to turn back toward the equator at a lower latitude and, in turn, leading to a phase shift of the NAO.

This result provides further evidence that changes in the mean atmospheric circulation will also affect ENSO teleconnections in future

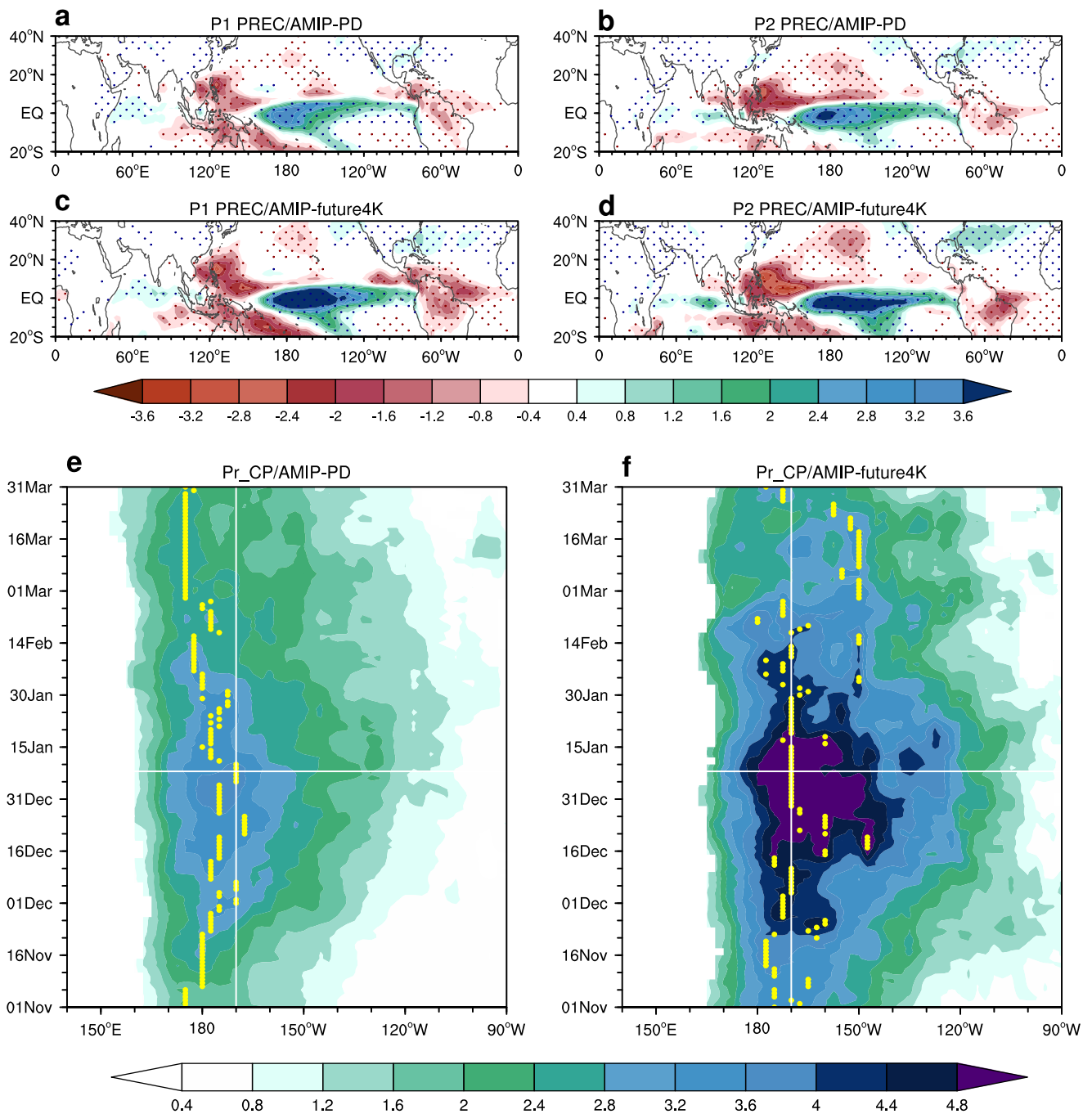


Fig. 3 | Enhanced and eastward-shifted ENSO tropical convection in the future. Regression coefficients of the (a) P1 and (b) P2 precipitation anomalies (shadings in mm/day) with respect to the DJF Niño-3.4 index for the MME of AMIP-PD simulations. c, d are the same as (a, b) but for the MME of AMIP-future4K simulations. The dots denote that the corresponding anomalies are significant at the 90% confidence level. Regression coefficients of the tropical central-eastern Pacific meridional mean (5°S–5°N) daily precipitation anomalies with respect to the DJF

Niño-3.4 index for the MME of (e) AMIP-PD and (f) AMIP-future4K simulations. Note that only the significant positive values at the 90% confidence level are displayed. The yellow dot represents the zonal location of the maximum regression coefficient at each calendar day. The horizontal white line separates the whole winter period into early (P1) and late winter (P2). The vertical white line marks the 170°W longitude for better comparison.

projections⁶¹. In P2, the climatological jet meridional shear also shows a similar weakening trend (Supplementary Fig. 3). However, the PD jet meridional shear is already weak enough to make the anomaly display a northeast–southwest tilt direction. Further weakening of the jet meridional shear does not produce distinct change in the Rossby wave propagating direction over the North American region.

According to previous studies, in addition to tropospheric mechanisms, late winter ENSO influence on the NAO is also related to stratospheric processes: Enhanced central-eastern Pacific convection during El Niño is

linked to a deeper Aleutian Low, a weaker stratospheric polar vortex, and thus a negative NAO^{19,62}. We then examine the possible change of this mechanism by showing the time evolution of the upward propagation of the planetary waves (Supplementary Fig. 4) and the vertical profile of ENSO-regressed zonal wind anomaly at 60°N (Fig. 7a, b). It can be seen that the upward propagation of planetary waves into the stratosphere occurs earlier than the NAO phase transition shown in Fig. 1b, c, and the easterly wind anomalies, which implies a weakened polar vortex, appear mostly during P2 and can propagate downward to affect the tropospheric NAO during this

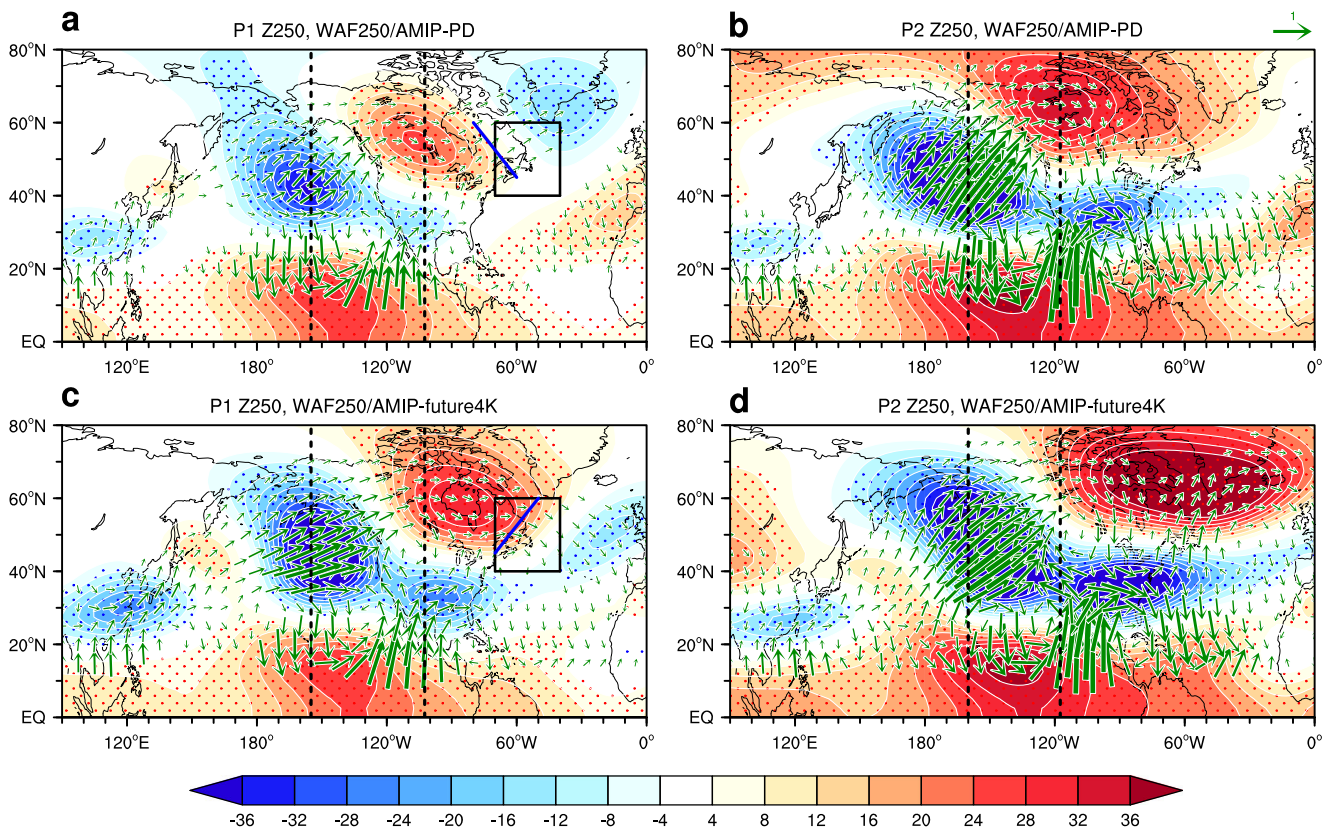


Fig. 4 | Enhanced and eastward-shifted ENSO extratropical atmospheric teleconnections in the future. Regression coefficients of (a) P1 and (b) P2 250-hPa geopotential height anomalies (shadings and contours in m) with respect to the DJF Niño-3.4 index and the associated wave activity flux (WAF, vectors in m^2s^{-2}) for the MME of the AMIP-PD simulations. (c)-(d) are the same as (a)-(b) but for the MME of AMIP-future4K simulations. The black box ($40^\circ\text{--}60^\circ\text{N}$, $40^\circ\text{--}70^\circ\text{W}$) outlines the area that features distinct Rossby wave-propagating directions in P1 between the two

simulations. The blue lines in (a) and (c) roughly denote the tilt direction of the atmospheric anomaly over northeastern North America. Dots are displayed when the geopotential height anomalies are significant at the 90% confidence level. For better comparison, the vertical black dashed lines are drawn to mark the central longitudes of the ENSO-regressed Aleutian low and the positive geopotential height anomalies over northeastern North America, respectively. The WAF is shown only when its magnitude is larger than $0.05 \text{ m}^2\text{s}^{-2}$.

period. Compared to the linkage in the PD, the easterly wind anomaly, as well as the downward propagation of this signal, is clearly stronger in the AMIP-future4K simulations, suggesting a future intensification of this pathway. Previous studies suggested that “low-top” models (with model top pressure $>1 \text{ hPa}$) cannot realistically simulate the Arctic stratospheric response to ENSO^{64,65}. We exclude the two “low-top” model simulations (Supplementary Table 1) and the result remains qualitatively unchanged (Supplementary Fig. 5).

It is well known that ENSO disturbs the polar stratospheric circulation by means of planetary Rossby waves^{29,66,67}. To clarify how the stratospheric pathway is enhanced in the future, we next examine and compare the features of upward planetary wave activities in the two experiments. Figure 7c, d display the wavenumber-1 component of the ENSO-regressed wintertime geopotential height anomalies at 50-hPa, as compared to the wavenumber-1 component of the climatological stationary wave, in the AMIP-PD and AMIP-future4K simulations, respectively. Here, we focus on the 50-hPa pressure level, though the choice of other levels between the upper troposphere and lower stratosphere yields the same results. It can be seen that, in both simulations, the wavenumber-1 height anomaly is basically in phase with the climatology, suggesting that the upward propagation of the wavenumber-1 EP flux anomalies from the extratropical troposphere to the stratosphere is generally enhanced (Fig. 7e). This is consistent with many previous studies^{19,29,68,69}. However, compared to that in the AMIP-PD simulations, the ENSO-regressed wavenumber-1 height anomaly in the AMIP-future4K simulations shows much stronger amplitude and better agreement with the climatology due to the enhanced and eastward-shifted tropical convection response to ENSO (Fig. 7d). Correspondingly, there is a

stronger upward propagation of the wavenumber-1 EP flux anomalies from the mid to high latitude troposphere into the stratosphere in the future (Fig. 7e). Meanwhile, we also find that the upward propagations of the wavenumber-2 and wavenumber-3 EP flux anomalies are respectively weakened and strengthened in the AMIP-future4K simulations compared to the AMIP-PD simulations. However, these changes are relatively minor and the change in upward propagation of EP flux is mostly contributed by the wavenumber-1 component.

Discussion

The winter ENSO-NAO teleconnection has garnered substantial attention in historical and modern climates^{6,70,71}. Despite high uncertainty, both observational and modelling analyses have shown a subseasonal transition of the ENSO-NAO phase relationship from positive to negative in early January^{14,16,17}. In this study, we investigate the future changes of this teleconnection utilizing two sets of atmospheric model simulations from CMIP6. Namely, the AMIP-PD simulation forced by observed PD SST, and the AMIP-future4K simulation forced by the same SST plus spatially patterned future SST warming. The results show that while the PD positive early winter ENSO-NAO correlation apparently weakens and shifts to negative in the future, the current negative ENSO-NAO relationship in late winter strengthens under future greenhouse warming. In other words, there is a projected tendency towards a more negative NAO anomaly throughout the ENSO winter. In the future, the PD subseasonal reversal of the ENSO-NAO teleconnection is expected to disappear. Additionally, the surface climate response to ENSO over the Euro-Atlantic region exhibits a consistent feature from the PD to the future under greenhouse warming.

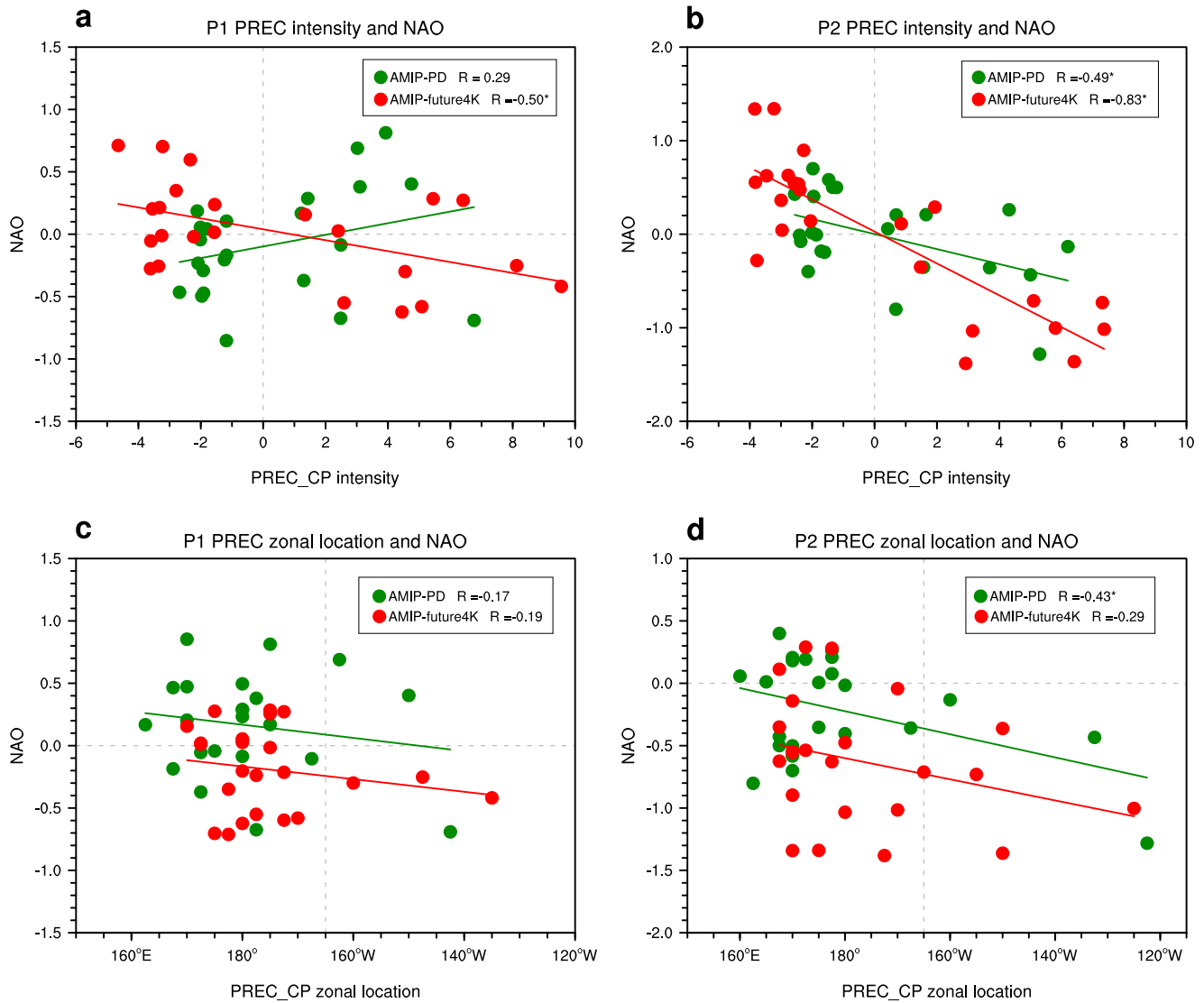


Fig. 5 | Strengthened and east-shifted ENSO tropical convection anomalies favor a more negative NAO response. Scatterplot of the intensity of the tropical (5°S–5°N) central-eastern Pacific precipitation anomaly and the NAO index during the (a) P1 and (b) P2 of ENSO winters for the AMIP-PD (red dots) and AMIP-future4K (green dots) simulations with the corresponding linear regression lines. The corresponding correlation coefficients (*R*) are also displayed and the asterisk indicates significance at the 90% confidence level. c–d are the same as (a–b), but for

the scatterplot between the zonal location of the tropical central-eastern Pacific precipitation anomaly and the NAO index. The zonal location is defined as the longitude of the maximum absolute precipitation anomaly in the tropical (5°S–5°N) central-eastern Pacific during a certain ENSO early or late winter. Note that the signs of the NAO indices during La Niña winters in (c–d) are reversed to show the linear relationship.

As the mechanism responsible for the ENSO-NAO teleconnection in early winter is generally recognized to be different from that in late winter, we investigate the linking pathway for each period separately. Specifically, two factors are proposed to contribute to the weakening of the NAO response in early winter. One is the weakening of the North Atlantic jet meridional shear, which shifts the ENSO-driven Rossby wave-propagating direction from northeast to southeast over northeastern North America, thus reducing the positive NAO anomaly. The second factor involves the strengthening and eastward migration of the ENSO-induced tropical convection and extratropical atmospheric Rossby wave train, which facilitate the development of a negative NAO. During late winter, the mechanism regarding changes in the intensity and zonal location of the ENSO-induced Rossby wave train remains active on the ENSO-NAO teleconnection future change. Furthermore, the stratospheric pathway involving a deepened Aleutian low and a weakened stratospheric polar vortex is also reinforced in the future due to the significant intensification of the upward EP flux of the wavenumber-1 wave, resulting in a stronger downward impact on the NAO.

Our finding of a future strengthening of the late-winter ENSO-NAO relationship is consistent with previous studies^{40,41,43,44}. They also suggest that this is due to the stronger and more eastward shifting tropical convection in response to ENSO^{44,72,73}, which modulates the extratropical atmospheric teleconnection over the North Pacific and North America to show a parallel change. However, we further show here that the early winter NAO and the subseasonally varying NAO response to ENSO are projected to weaken in a warming climate, which may offer an avenue for better understanding and projection of the future climate change in the Euro-Atlantic region.

Further research is necessary to obtain a better understanding of this scientific issue. For example, although several mechanisms have been proposed in this paper to understand the future changes of the teleconnection, they primarily rely on qualitative analyses, dedicated model experiments are needed to fully assess the teleconnection pathways and their relative importance. This study primarily analyzes the ENSO-NAO relationship from a linear perspective, the nonlinear and asymmetric features embedded in this teleconnection^{11,74,75} and its future change is also a worthwhile topic to

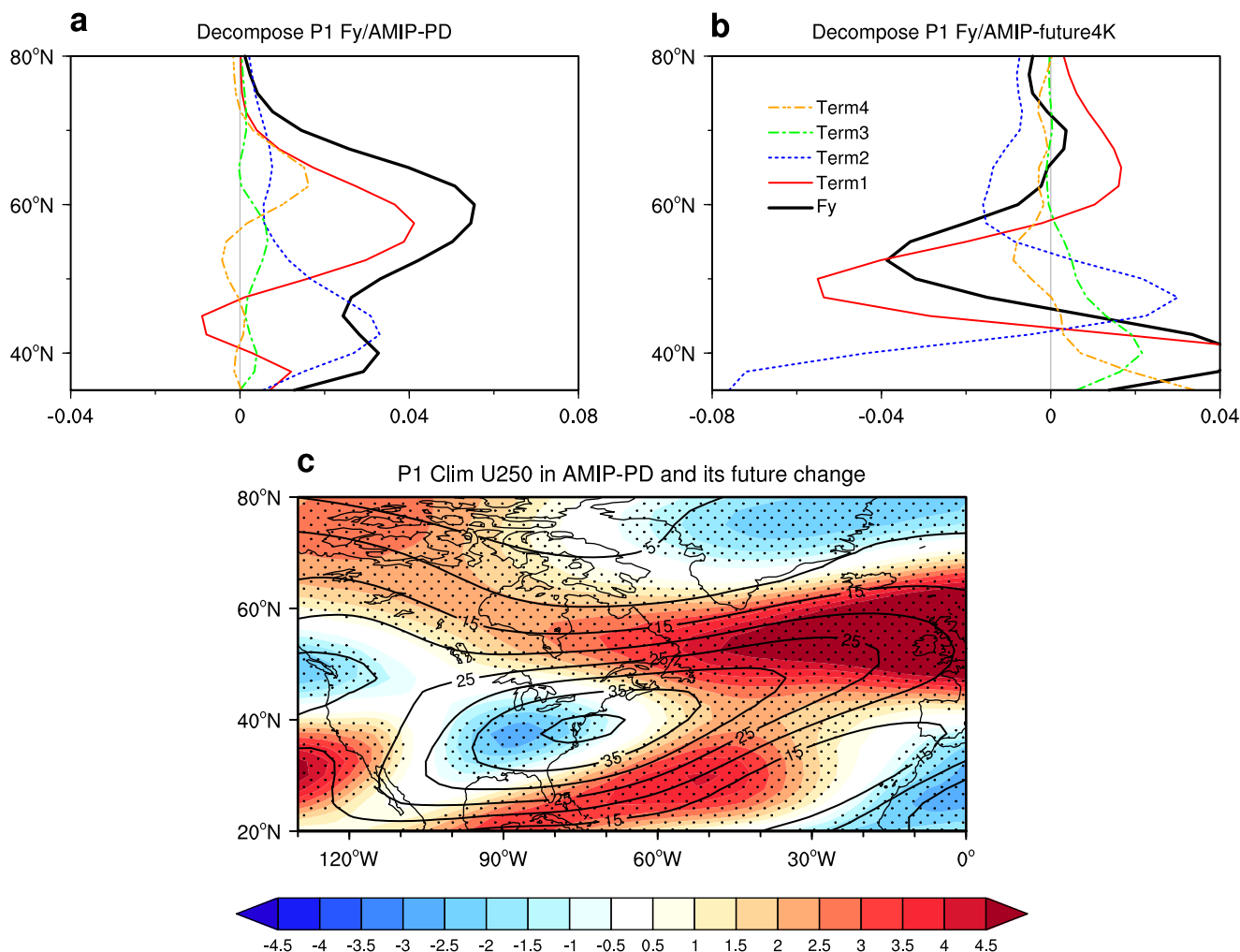


Fig. 6 | Climatological weakening of the North Atlantic jet meridional shear shifts the Rossby wave-propagating direction. Latitudinal distributions of the meridional component of 250-hPa WAF (F_y) during P1 and its four constituents (curves in $m^2 s^{-2}$) with respect to the DJF Niño-3.4 index over the northeastern North American region ($40^\circ\text{--}60^\circ\text{N}$, $40^\circ\text{--}70^\circ\text{W}$) for the MME of the (a) AMIP-PD and (b) AMIP-future4K

simulations. c Spatial pattern of climatological 250-hPa zonal wind (contours in $m s^{-1}$) during P1 for the MME of the AMIP-PD simulations. The shadings (units: $m s^{-1}$) show the P1 climatological 250-hPa zonal wind differences between the MME of the AMIP-future4K and AMIP-PD simulations. The dots denote the zonal wind differences that are significant at the 90% confidence level.

investigate. We consider the future change in the ENSO atmospheric teleconnection only as the response of the CO_2 -induced SST warming pattern. The possible effect of the direct CO_2 forcing on the atmospheric change also needs to be clarified.

Methods

Re-analysis products

Reanalysis datasets are used in this study as a reference to describe the performance of the AMIP simulations on the PD ENSO-NAO teleconnection. The monthly SST datasets (1979–2014) are derived from the National Oceanic and Atmospheric Administration extended reconstructed SSTV5 data⁷⁶. Daily atmospheric circulation datasets during the same period are derived from the fifth generation of the European Centre for Medium-Range Weather Forecasts re-analysis (ERA-5)⁷⁷. The SST dataset from the Hadley Centre (HadISST)⁷⁸ is also examined and results remain unchanged.

We primarily focus on the analysis for the boreal winter season (November–March, NDJFM) in a broad sense, and the winter of 1979 refers to the winter of 1979/1980. A linear trend was removed to avoid possible influences associated with long-term trends. Anomalies were derived relative to the daily mean climatology over the entire study period. We also perform a 9-day running mean to exclude any possible noise disturbances

caused by synoptic variability. Several indices are defined to facilitate our analyses. The NAO index is defined by the difference in normalized SLP anomalies between 35°N and 65°N over the North Atlantic sector (zonally averaged from 80°W to 30°E)⁷⁹. ENSO events are identified based on a threshold of ± 0.5 standard deviations of the December to February (DJF) average Niño-3.4 index (averaged SST anomaly in the domain of $5^\circ\text{S}\text{--}5^\circ\text{N}$, $120^\circ\text{--}170^\circ\text{W}$). With this method, during the target period, we can obtain 10 El Niño years: 1982, 1986, 1987, 1991, 1994, 1997, 2002, 2004, 2006, and 2009; and 13 La Niña years: 1983, 1984, 1985, 1988, 1995, 1998, 1999, 2000, 2005, 2007, 2008, 2010, and 2011.

Multi-model CMIP6 simulations

The AMIP-PD and AMIP-future4K experiments performed by the atmospheric general circulation models (AGCMs) participating in CMIP6 are adopted to examine the future change in the wintertime ENSO-NAO teleconnection. Seven models are used (Supplementary Table 1) as they can provide all the required variables for these two experiments. The AMIP-PD experiment is forced by observed PD monthly SST from 1979 to 2014. Other external forcings, including volcanic aerosols, solar variability, greenhouse gas concentrations, and anthropogenic aerosols are prescribed consistent with those used in the CMIP6 historical simulation⁸⁰. The boundary forcing of the

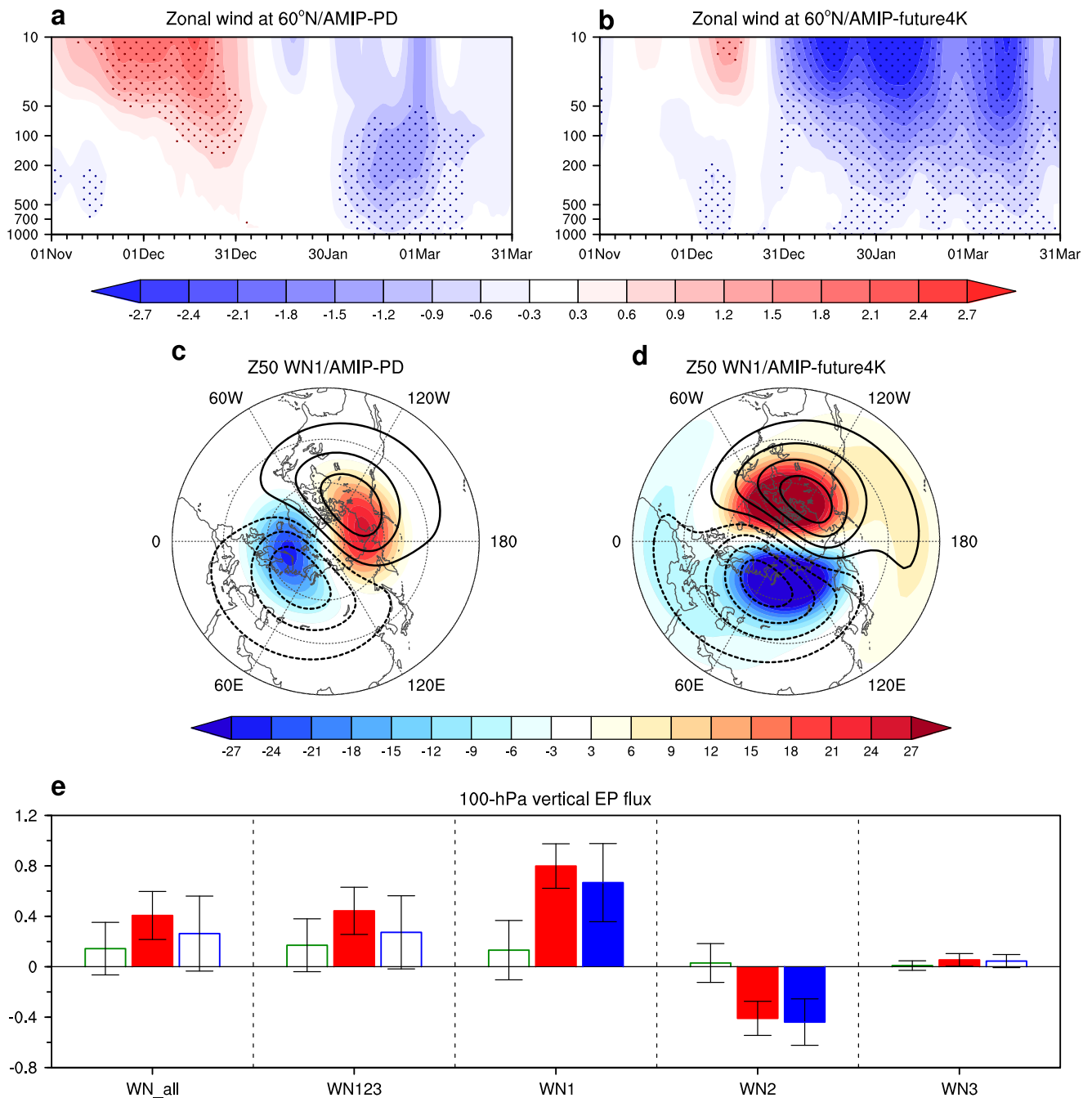


Fig. 7 | An enhanced stratospheric pathway favors a future strengthening of the ENSO-NAO teleconnection in late winter. Regression coefficients of the wintertime daily zonal wind anomalies (shadings in ms^{-1}) at 60°N with respect to the DJF Niño-3.4 index from 1000 to 10 hPa for the MME of the (a) AMIP-PD and (b) AMIP-future4K simulations. The dots denote the zonal wind anomalies that are significant at the 90% confidence level. The wavenumber-1 components of the regressed wintertime 50-hPa geopotential height anomalies (shadings in m) with respect to the DJF Niño-3.4 index for the MME of the (c) AMIP-PD and (d) AMIP-

future4K simulations. Contours indicate the corresponding climatological planetary wavenumber-1 components that are shown at ± 30 , ± 60 , ± 90 , and ± 150 m. **e** Regression coefficients of the vertical component of 100-hPa EP flux (bars in $10^5 \text{ Pa m}^2 \text{ s}^{-2}$) of different wavenumbers averaged in 60°–80°N for the MME of the AMIP-PD (green bar) and AMIP-future4K (red bar) simulations and the differences between AMIP-future4K and AMIP-PD simulations (blue bar). Error bars represent the 90% confidence interval. The solid bar denotes that the corresponding regression is significant at the 90% confidence level.

AMIP-future4K experiment is the same as AMIP-PD but with a projected spatially patterned SST warming (Supplementary Fig. 6) added. The spatial pattern of SST change is obtained from the SST response of 13 CMIP3 coupled models to CO_2 quadrupling⁸¹. The amplitude of globally (ice-free region) averaged SST warming has been adjusted to 4K. The comparison of the ENSO-NAO teleconnection in the AMIP-future4K with that in the AMIP-PD experiments yields the effects of the greenhouse warming-induced

SST pattern change on the teleconnection. All of the model data are bilinearly interpolated onto a common $2.5^\circ \times 2.5^\circ$ grid before analysis.

WAF

To analyze the source and direction of wave energy propagation, the wave activity flux (WAF) developed by Takaya and Nakamura⁸² is applied. The WAF is parallel to the local group velocity that corresponds to the stationary Rossby waves and is independent of the wave phase⁸². It has been considered

a useful tool for supplying information about wave propagation and is defined as:

$$F = \frac{p \cos \phi}{2|U|} \left\{ \begin{aligned} & \frac{U}{a^2 \cos^2 \phi} \left[\left(\frac{\partial \psi'}{\partial \lambda} \right)^2 - \psi' \frac{\partial^2 \psi'}{\partial \lambda^2} \right] + \frac{V}{a^2 \cos \phi} \left(\frac{\partial \psi'}{\partial \lambda} \frac{\partial \psi'}{\partial \phi} - \psi' \frac{\partial^2 \psi'}{\partial \lambda \partial \phi} \right) \\ & \frac{U}{a^2 \cos \phi} \left(\frac{\partial \psi'}{\partial \lambda} \frac{\partial \psi'}{\partial \phi} - \psi' \frac{\partial^2 \psi'}{\partial \lambda \partial \phi} \right) + \frac{V}{a^2} \left[\left(\frac{\partial \psi'}{\partial \phi} \right)^2 - \psi' \frac{\partial^2 \psi'}{\partial \phi^2} \right] \end{aligned} \right. \quad (1)$$

where p is the pressure normalized by 1000 hPa, a is Earth's radius, ϕ is the latitude and λ is the longitude. The geostrophic stream function ψ is defined as z/f , where z is the geopotential, and $f (=2\Omega \sin \phi)$ is the Coriolis parameter with the Earth's rotation rate (Ω). Also, $|U|$, U , and V represent the basic states of wind speed and zonal and meridional wind, whereas ψ' denotes the perturbed stream function. To explore the reasons for the changes in the WAF meridional component, we decompose F_y into four components, as follows:

$$F_y = \underbrace{\frac{pU}{2a^2|U|} \frac{\partial \psi'}{\partial \lambda} \frac{\partial \psi'}{\partial \phi}}_{\text{term 1}} - \underbrace{\frac{pU}{2a^2|U|} \psi' \frac{\partial^2 \psi'}{\partial \lambda \partial \phi}}_{\text{term 2}} + \underbrace{\frac{pV \cos \phi}{2a^2|U|} \left(\frac{\partial \psi'}{\partial \phi} \right)^2}_{\text{term 3}} - \underbrace{\frac{pV \cos \phi}{2a^2|U|} \psi' \frac{\partial^2 \psi'}{\partial \phi^2}}_{\text{term 4}} \\ = \underbrace{-\frac{pU \cos \phi}{2|U|} u' v'}_{\text{term 1}} - \underbrace{\frac{pU \cos \phi}{2a|U|} \psi' \frac{\partial v'}{\partial \phi}}_{\text{term 2}} + \underbrace{\frac{pV \cos \phi}{2|U|} u'^2}_{\text{term 3}} + \underbrace{\frac{pV \cos \phi}{2a|U|} \psi' \frac{\partial u'}{\partial \phi}}_{\text{term 4}} \quad (2)$$

EP flux

We use Eliassen-Palm (EP) flux to diagnose the planetary wave activities⁸³. The EP flux can be written as:

$$EP = \begin{cases} EP_\phi = -R \cos \phi \overline{u'v'} \\ EP_p = Rf \cos \phi \frac{\overline{v'\theta'}}{\theta_p} \end{cases} \quad (3)$$

in which Rf , ϕ , and θ are the Earth's radius, Coriolis parameter, latitude, and potential temperature, respectively. Overbars signify the zonal mean over a given zonal range, and primes signify departures therefrom. The horizontal component of the EP flux, EP_ϕ , is proportional to the meridional eddy momentum transport, and the vertical component EP_p represents the meridional eddy heat transport and is used to display the characteristics of the upward wave energy. The zonal Fourier harmonics are used to calculate the different wavenumber components of the EP flux. The EP flux is calculated at a daily time step and a seasonal mean is then obtained by averaging the daily results.

Statistical significance test

All our results are tested based on the two-sided Student's t -test.

Data availability

All the reanalysis data used in this study are publicly available and can be downloaded from the corresponding websites. ERA5: <https://www.ecmwf.int/en/forecasts/datasets/reanalysis-datasets/era5>; ERSSTv5: <https://psl.noaa.gov/data/gridded/data.noaa.ersst.v5.html>. The AMIP and AMIP-future4K model data used in this study can be obtained from the CMIP6 archives at <https://esgf-node.llnl.gov/search/cmip6/>.

Code availability

The code for the analysis in this paper is available from the first or corresponding authors upon reasonable request.

Received: 15 November 2023; Accepted: 15 March 2024;

Published online: 28 March 2024

References

- McPhaden, M. J., Zebiak, S. E. & Glantz, M. H. ENSO as an Integrating Concept in Earth Science. *Science* **314**, 1740–1745 (2006).
- Ropelewski, C. F. & Halpert, M. S. Global and Regional Scale Precipitation Patterns Associated with the El Niño/Southern Oscillation. *Mon. Wea. Rev.* **115**, 1606–1626 (1987).
- Brönnimann, S. Impact of El Niño–Southern Oscillation on European climate. *Rev. Geophys.* **45**, RG3003 (2007).
- Scaife, A. A. et al. Tropical rainfall, Rossby waves and regional winter climate predictions. *Q. J. R. Meteorol. Soc.* **143**, 1–11 (2017).
- López-Parages, J., Rodríguez-Fonseca, B. & Terray, L. A mechanism for the multidecadal modulation of ENSO teleconnection with Europe. *Clim. Dyn.* **45**, 867–880 (2015).
- Zhang, W. et al. Impact of ENSO longitudinal position on teleconnections to the NAO. *Clim. Dyn.* **52**, 257–274 (2019).
- Gouirand, I. & Moron, V. Variability of the impact of El Niño–southern oscillation on sea-level pressure anomalies over the North Atlantic in January to March. *Int. J. Climatol.* **23**, 1549–1566 (2003).
- Deser, C., Simpson, I. R., McKinnon, K. A. & Phillips, A. S. The Northern Hemisphere Extratropical Atmospheric Circulation Response to ENSO: How Well Do We Know It and How Do We Evaluate Models Accordingly? *J. Clim.* **30**, 5059–5082 (2017).
- Toniazzo, T. & Scaife, A. A. The influence of ENSO on winter North Atlantic climate. *Geophys. Res. Lett.* **33**, L24704 (2006).
- Hardiman, S. C. et al. The Impact of Strong El Niño and La Niña Events on the North Atlantic. *Geophys. Res. Lett.* **46**, 2874–2883 (2019).
- Jiménez-Esteve, B. & Domeisen, D. I. V. Nonlinearity in the North Pacific Atmospheric Response to a Linear ENSO Forcing. *Geophys. Res. Lett.* **46**, 2271–2281 (2019).
- Graf, H.-F. & Zanchettin, D. Central Pacific El Niño, the “subtropical bridge,” and Eurasian climate. *J. Geophys. Res.* **117**, D01102 (2012).
- Zhang, W., Wang, L., Xiang, B., Qi, L. & He, J. Impacts of two types of La Niña on the NAO during boreal winter. *Clim. Dyn.* **44**, 1351–1366 (2015).
- Moron, V. & Gouirand, I. Seasonal modulation of the El Niño–southern oscillation relationship with sea level pressure anomalies over the North Atlantic in October–March 1873–1996. *Int. J. Climatol.* **23**, 143–155 (2003).
- Ayarzagüena, B., Ineson, S., Dunstone, N. J., Baldwin, M. P. & Scaife, A. A. Intraseasonal Effects of El Niño–Southern Oscillation on North Atlantic Climate. *J. Clim.* **31**, 8861–8873 (2018).
- Abid, M. A. et al. Separating the Indian and Pacific Ocean Impacts on the Euro-Atlantic Response to ENSO and Its Transition from Early to Late Winter. *J. Clim.* **34**, 1531–1548 (2021).
- Joshi, M. K., Abid, M. A. & Kucharski, F. The Role of an Indian Ocean Heating Dipole in the ENSO Teleconnection to the North Atlantic European Region in Early Winter during the Twentieth Century in Reanalysis and CMIP5 Simulations. *J. Clim.* **34**, 1047–1060 (2021).
- Geng, X., Zhao, J. & Kug, J.-S. ENSO-driven abrupt phase shift in North Atlantic oscillation in early January. *NPJ Clim. Atmos. Sci.* **6**, 1–8 (2023).
- Ineson, S. & Scaife, A. A. The role of the stratosphere in the European climate response to El Niño. *Nat. Geosci.* **2**, 32–36 (2009).
- Jiménez-Esteve, B. & Domeisen, D. I. V. The Tropospheric Pathway of the ENSO–North Atlantic Teleconnection. *J. Clim.* **31**, 4563–4584 (2018).
- Bladé, I., Newman, M., Alexander, M. A. & Scott, J. D. The Late Fall Extratropical Response to ENSO: Sensitivity to Coupling and Convection in the Tropical West Pacific. *J. Clim.* **21**, 6101–6118 (2008).
- Li, R. K. K., Woollings, T., O'Reilly, C. & Scaife, A. A. Effect of the North Pacific Tropospheric Waveguide on the Fidelity of Model El Niño Teleconnections. *J. Clim.* **33**, 5223–5237 (2020).
- Kug, J.-S. & Jin, F.-F. Left-hand rule for synoptic eddy feedback on low-frequency flow. *Geophys. Res. Lett.* **36**, L05709 (2009).

24. Kug, J.-S., Jin, F.-F., Park, J., Ren, H.-L. & Kang, I.-S. A general rule for synoptic-eddy feedback onto low-frequency flow. *Clim. Dyn.* **35**, 1011–1026 (2010).
25. Sung, M.-K., Ham, Y.-G., Kug, J.-S. & An, S.-I. An alternative effect by the tropical North Atlantic SST in intraseasonally varying El Niño teleconnection over the North Atlantic. *Tellus A* **65**, 19863 (2013).
26. Ham, Y.-G., Sung, M.-K., An, S.-I., Schubert, S. D. & Kug, J.-S. Role of tropical Atlantic SST variability as a modulator of El Niño teleconnections. *Asia Pac. J. Atmos. Sci.* **50**, 247–261 (2014).
27. Maidens, A., Knight, J., Martin, N. & Andrews, M. Contrasting Conditions in the U.K. Winter of 2015/16 as a Result of Remote Tropical Influences. *J. Clim.* **32**, 3227–3243 (2019).
28. Li, Y. & Lau, N.-C. Impact of ENSO on the Atmospheric Variability over the North Atlantic in Late Winter—Role of Transient Eddies. *J. Clim.* **25**, 320–342 (2012).
29. Manzini, E., Giorgetta, M. A., Esch, M., Kornblueh, L. & Roeckner, E. The Influence of Sea Surface Temperatures on the Northern Winter Stratosphere: Ensemble Simulations with the MAECHAM5 Model. *J. Clim.* **19**, 3863–3881 (2006).
30. Cagnazzo, C. & Manzini, E. Impact of the Stratosphere on the Winter Tropospheric Teleconnections between ENSO and the North Atlantic and European Region. *J. Clim.* **22**, 1223–1238 (2009).
31. Bell, C. J., Gray, L. J., Charlton-Perez, A. J., Joshi, M. M. & Scaife, A. A. Stratospheric Communication of El Niño Teleconnections to European Winter. *J. Clim.* **22**, 4083–4096 (2009).
32. Iza, M., Calvo, N. & Manzini, E. The Stratospheric Pathway of La Niña. *J. Clim.* **29**, 8899–8914 (2016).
33. Kug, J.-S., An, S.-I., Ham, Y.-G. & Kang, I.-S. Changes in El Niño and La Niña teleconnections over North Pacific–America in the global warming simulations. *Theor. Appl. Climatol.* **100**, 275–282 (2010).
34. Power, S., Delage, F., Chung, C., Kociuba, G. & Keay, K. Robust twenty-first-century projections of El Niño and related precipitation variability. *Nature* **502**, 541–545 (2013).
35. Watanabe, M., Kamae, Y. & Kimoto, M. Robust increase of the equatorial Pacific rainfall and its variability in a warmed climate. *Geophys. Res. Lett.* **41**, 3227–3232 (2014).
36. Yan, Z. et al. Eastward shift and extension of ENSO-induced tropical precipitation anomalies under global warming. *Sci. Adv.* **6**, eaax4177 (2020).
37. Hu, K., Huang, G., Huang, P., Kosaka, Y. & Xie, S.-P. Intensification of El Niño-induced atmospheric anomalies under greenhouse warming. *Nat. Geosci.* 1–6 <https://doi.org/10.1038/s41561-021-00730-3> (2021).
38. Cai, W. et al. Increasing frequency of extreme El Niño events due to greenhouse warming. *Nat. Clim. Change* **4**, 111–116 (2014).
39. Cai, W. et al. Increased frequency of extreme La Niña events under greenhouse warming. *Nat. Clim. Change* **5**, 132–137 (2015).
40. Fereday, D. R., Chadwick, R., Knight, J. R. & Scaife, A. A. Tropical Rainfall Linked to Stronger Future ENSO-NAO Teleconnection in CMIP5 Models. *Geophys. Res. Lett.* **47**, e2020GL088664 (2020).
41. Herceg Bulić, I., Branković, Č. & Kucharski, F. Winter ENSO teleconnections in a warmer climate. *Clim. Dyn.* **38**, 1593–1613 (2012).
42. Müller, W. A. & Roeckner, E. ENSO impact on midlatitude circulation patterns in future climate change projections. *Geophys. Res. Lett.* **33**, L05711 (2006).
43. Müller, W. A. & Roeckner, E. ENSO teleconnections in projections of future climate in ECHAM5/MPI-OM. *Clim. Dyn.* **31**, 533–549 (2008).
44. Drouard, M. & Cassou, C. A Modeling- and Process-Oriented Study to Investigate the Projected Change of ENSO-Forced Wintertime Teleconnectivity in a Warmer World. *J. Clim.* **32**, 8047–8068 (2019).
45. Taschetto, A. S. et al. Cold Tongue and Warm Pool ENSO Events in CMIP5: Mean State and Future Projections. *J. Clim.* **27**, 2861–2885 (2014).
46. Jiang, W., Huang, P., Huang, G. & Ying, J. Origins of the Excessive Westward Extension of ENSO SST Simulated in CMIP5 and CMIP6 Models. *J. Clim.* **34**, 2839–2851 (2021).
47. Lin, Y.-S., Wang, L.-C. & Li, J.-L. F. Effects of Equatorial Ocean Current Bias on Simulated El Niño Pattern in CMIP6 Models. *Geophys. Res. Lett.* **50**, e2023GL102890 (2023).
48. Bayr, T., Domeisen, D. I. V. & Wengel, C. The effect of the equatorial Pacific cold SST bias on simulated ENSO teleconnections to the North Pacific and California. *Clim. Dyn.* **53**, 3771–3789 (2019).
49. Jiang, W. et al. Biases and improvements of the ENSO-East Asian winter monsoon teleconnection in CMIP5 and CMIP6 models. *Clim. Dyn.* **59**, 2467–2480 (2022).
50. Williams, N. C., Scaife, A. A. & Screen, J. A. Underpredicted ENSO Teleconnections in Seasonal Forecasts. *Geophys. Res. Lett.* **50**, e2022GL101689 (2023).
51. King, M. P. et al. Importance of Late Fall ENSO Teleconnection in the Euro-Atlantic Sector. *Bull. Am. Meteor. Soc.* **99**, 1337–1343 (2018).
52. King, M. P., Herceg-Bulić, I., Kucharski, F. & Keenlyside, N. Interannual tropical Pacific sea surface temperature anomalies teleconnection to Northern Hemisphere atmosphere in November. *Clim. Dyn.* **50**, 1881–1899 (2018).
53. Hurrell, J. W., Kushnir, Y., Ottersen, G. & Visbeck, M. An overview of the North Atlantic Oscillation. In *Geophysical Monograph Series* (eds. Hurrell, J. W., Kushnir, Y., Ottersen, G. & Visbeck, M.) vol. 134 1–35 (American Geophysical Union), (2003).
54. Scaife, A. A., Folland, C. K., Alexander, L. V., Moberg, A. & Knight, J. R. European Climate Extremes and the North Atlantic Oscillation. *J. Clim.* **21**, 72–83 (2008).
55. Hoskins, B. J. & Karoly, D. J. The Steady Linear Response of a Spherical Atmosphere to Thermal and Orographic Forcing. *J. Atmos. Sci.* **38**, 1179–1196 (1981).
56. Trenberth, K. E. et al. Progress during TOGA in understanding and modeling global teleconnections associated with tropical sea surface temperatures. *J. Geophys. Res.* **103**, 14291–14324 (1998).
57. Barnes, E. A. & Polvani, L. Response of the Midlatitude Jets, and of Their Variability, to Increased Greenhouse Gases in the CMIP5 Models. *J. Clim.* **26**, 7117–7135 (2013).
58. Simpson, I. R., Shaw, T. A. & Seager, R. A Diagnosis of the Seasonally and Longitudinally Varying Midlatitude Circulation Response to Global Warming. *J. Atmos. Sci.* **71**, 2489–2515 (2014).
59. Ceppi, P., Zappa, G., Shepherd, T. G. & Gregory, J. M. Fast and Slow Components of the Extratropical Atmospheric Circulation Response to CO₂ Forcing. *J. Clim.* **31**, 1091–1105 (2018).
60. Hoskins, B. J. & Ambrizzi, T. Rossby Wave Propagation on a Realistic Longitudinally Varying Flow. *J. Atmos. Sci.* **50**, 1661–1671 (1993).
61. Yeh, S.-W. et al. ENSO Atmospheric Teleconnections and Their Response to Greenhouse Gas Forcing. *Rev. Geophys.* **56**, 185–206 (2018).
62. Domeisen, D. I. V., Garfinkel, C. I. & Butler, A. H. The Teleconnection of El Niño Southern Oscillation to the Stratosphere. *Rev. Geophys.* **57**, 5–47 (2019).
63. Charlton-Perez, A. J. et al. On the lack of stratospheric dynamical variability in low-top versions of the CMIP5 models. *J. Geophys. Res.* **118**, 2494–2505 (2013).
64. Calvo, N. et al. Northern Hemisphere Stratospheric Pathway of Different El Niño Flavors in Stratosphere-Resolving CMIP5 Models. *J. Clim.* **30**, 4351–4371 (2017).
65. Hurwitz, M. M. et al. Extra-tropical atmospheric response to ENSO in the CMIP5 models. *Clim. Dyn.* **43**, 3367–3376 (2014).
66. Hoerling, M. P., Kumar, A. & Zhong, M. El Niño, La Niña, and the Nonlinearity of Their Teleconnections. *J. Clim.* **10**, 1769–1786 (1997).
67. Garfinkel, C. I. & Hartmann, D. L. Different ENSO teleconnections and their effects on the stratospheric polar vortex. *J. Geophys. Res.* **113**, (2008).

68. Garfinkel, C. I., Hartmann, D. L. & Sassi, F. Tropospheric Precursors of Anomalous Northern Hemisphere Stratospheric Polar Vortices. *J. Clim.* **23**, 3282–3299 (2010).
69. Nishii, K., Nakamura, H. & Orsolini, Y. J. Cooling of the wintertime Arctic stratosphere induced by the western Pacific teleconnection pattern. *Geophys. Res. Lett.* **37**, (2010).
70. Rogers, J. C. The Association between the North Atlantic Oscillation and the Southern Oscillation in the Northern Hemisphere. *Mon. Wea. Rev.* **112**, 1999–2015 (1984).
71. Fraedrich, K. & Müller, K. Climate anomalies in Europe associated with ENSO extremes. *Int. J. Climatol.* **12**, 25–31 (1992).
72. Cai, W., Wang, G., Santoso, A., Lin, X. & Wu, L. Definition of Extreme El Niño and Its Impact on Projected Increase in Extreme El Niño Frequency. *Geophys. Res. Lett.* **44**, 11,184–11,190 (2017).
73. Meehl, G. A. & Teng, H. Multi-model changes in El Niño teleconnections over North America in a future warmer climate. *Clim. Dyn.* **29**, 779–790 (2007).
74. Trascasa-Castro, P., Maycock, A. C., Yiu, Y. Y. S. & Fletcher, J. K. On the Linearity of the Stratospheric and Euro-Atlantic Sector Response to ENSO. *J. Clim.* **32**, 6607–6626 (2019).
75. Jiménez-Esteve, B. & Domeisen, D. I. V. Nonlinearity in the tropospheric pathway of ENSO to the North Atlantic. *Weather Clim. Dyn.* **1**, 225–245 (2020).
76. Huang, B. et al. Extended Reconstructed Sea Surface Temperature, Version 5 (ERSSTv5): Upgrades, Validations, and Intercomparisons. *J. Clim.* **30**, 8179–8205 (2017).
77. Hersbach, H. et al. The ERA5 global reanalysis. *Q. J. R. Meteorol. Soc.* **146**, 1999–2049 (2020).
78. Rayner, N. A. et al. Global analyses of sea surface temperature, sea ice, and night marine air temperature since the late nineteenth century. *J. Geophys. Res. Atmos.* **108**, (2003).
79. Li, J. & Wang, J. X. L. A New North Atlantic Oscillation Index and Its Variability. *Adv. Atmos. Sci.* **20**, 661–676 (2003).
80. Eyring, V. et al. Overview of the Coupled Model Intercomparison Project Phase 6 (CMIP6) experimental design and organization. *Geosci. Model Dev.* **9**, 1937–1958 (2016).
81. Webb, M. J. et al. The Cloud Feedback Model Intercomparison Project (CFMIP) contribution to CMIP6. *Geosci. Model Dev.* **10**, 359–384 (2017).
82. Takaya, K. & Nakamura, H. A Formulation of a Phase-Independent Wave-Activity Flux for Stationary and Migratory Quasigeostrophic Eddies on a Zonally Varying Basic Flow. *J. Atmos. Sci.* **58**, 608–627 (2001).
83. Edmon, H. J., Hoskins, B. J. & McIntyre, M. E. Eliassen-Palm Cross Sections for the Troposphere. *J. Atmos. Sci.* **37**, 2600–2616 (1980).
- Science Foundation of China (42088101, 41905073). This work was also supported by the National Supercomputing Center with supercomputing resources, and associated technical support (KSC-2023-CHA-0001). Y.K. was supported by the Japan Society for the Promotion of Science through Grants-in-Aid for Scientific Research (JP19H05703, JP22H01299, JP23H01241, and JP23H01250) and by the Japanese Ministry of Education, Culture, Sports, Science and Technology program for the advanced studies of climate change projection (JPMXD0722680395) and ArCSII (JPMXD1420318865).

Author contributions

J.-S. Kug and X. Geng initiated the idea. X. Geng conducted analyses, prepared all the Figures, and wrote the initial draft of the paper. J.-S. Kug supervised and improved the whole work, formulated the design of the analyses, and developed the manuscript content. Y. Kosaka provided instructive insights on the analysis. All authors discussed the results and reviewed the manuscript.

Competing interests

The authors declare no competing interests.

Additional information

Supplementary information The online version contains supplementary material available at <https://doi.org/10.1038/s41612-024-00627-z>.

Correspondence and requests for materials should be addressed to Jong-Seong Kug.

Reprints and permissions information is available at <http://www.nature.com/reprints>

Publisher's note Springer Nature remains neutral with regard to jurisdictional claims in published maps and institutional affiliations.

Open Access This article is licensed under a Creative Commons Attribution 4.0 International License, which permits use, sharing, adaptation, distribution and reproduction in any medium or format, as long as you give appropriate credit to the original author(s) and the source, provide a link to the Creative Commons licence, and indicate if changes were made. The images or other third party material in this article are included in the article's Creative Commons licence, unless indicated otherwise in a credit line to the material. If material is not included in the article's Creative Commons licence and your intended use is not permitted by statutory regulation or exceeds the permitted use, you will need to obtain permission directly from the copyright holder. To view a copy of this licence, visit <http://creativecommons.org/licenses/by/4.0/>.

© The Author(s) 2024

Acknowledgements

This work was supported by the National Research Foundation of Korea (NRF-2022R1A3B1077622). X.G. was supported by National Natural